Article

An extended low-density atmosphere around the Jupiter-sized planet WASP-193 b

🔴 Check for updates

Khalid Barkaoui [1,2,3,4] ✉, Francisco J. Pozuelos [1,5] ✉, Coel Hellier[6], Barry Smalley [6], Louise D. Nielsen [7,8], Prajwal Niraula [3], Michaël Gillon [1], Julien de Wit [3], Simon Müller [9], Caroline Dorn [9], Ravit Helled [9], Emmanuel Jehin [10], Brice-Olivier Demory [11], Valerie Van Grootel [10], Abderahmane Soubkiou[2,12], Mourad Ghachoui[1,2], David. R. Anderson [13], Zouhair Benkhaldoun [2], Francois Bouchy [7], Artem Burdanov [3], Laetitia Delrez [1,10], Elsa Ducrot [14,15], Lionel Garcia [1,16], Abdelhadi Jabiri[2], Monika Lendl [7], Pierre F. L. Maxted [6], Catriona A. Murray [17], Peter Pihlmann Pedersen [18], Didier Queloz [7,18], Daniel Sebastian [19], Oliver Turner [7,20], Stephane Udry [7], Mathilde Timmermans [1], Amaury H. M. J. Triaud [19] & Richard G. West [13,21]

Gas giants transiting bright nearby stars provide crucial insights into planetary system formation and evolution mechanisms. Most of these planets show certain average characteristics, serving as benchmarks for our understanding of planetary systems. However, outliers like the planet we present in this study, WASP-193 b, offer unique opportunities to explore unconventional formation and evolution processes. This planet completes an orbit around its V-band-magnitude 12.2 F9 main-sequence host star every 6.25 days. Our analyses found that WASP-193 b has a mass of $0.139 \pm 0.029\,M_J$ and a radius of $1.464 \pm 0.058\,R_J$, translating into an extremely low density of $0.059 \pm 0.014\,\mathrm{g\,cm^{-3}}$, at least one order of magnitude less than standard gas giants like Jupiter. Typical gas giants such as Jupiter have densities that range between $0.2\,\mathrm{g\,cm^{-3}}$ and $2\,\mathrm{g\,cm^{-3}}$. The combination of its large transit depth (1.4%), extremely low density, high-equilibrium temperature (1,254 ± 31 K) and the infrared brightness of its host star (K-band magnitude 10.7) makes WASP-193 b an exquisite target for characterization by transmission spectroscopy (transmission spectroscopy metric ~600). One single JWST transit observation would yield detailed insights into its atmospheric properties and planetary mass, providing a unique window to explore the mechanisms behind its exceptionally low density and shed light on giant planets' diverse nature.

WASP-193 was observed by the WASP-South[1] survey in 2006–2008 and 2011–2012. The WASP photometry revealed a periodic signal consistent with transits of a giant planet with an orbital period of 6.25 d (Methods).

We used TRAPPIST-South[2] and SPECULOOS-South[3] ground-based telescopes to observe five transits of WASP-193 b, one in the I + z filter (02 January 2015), one in a 'blue-blocking' (BB) filter (06 April 2015), one in the Sloan-z' filter (27 January 2017) and two in the Johnson-B filter (08 June 2019). Additional photometric measurements were collected by the TESS[4] mission with 1,800 s, 600 s and 120 s cadences, of which we used in our analysis the Presearch Data Conditioning Simple Aperture
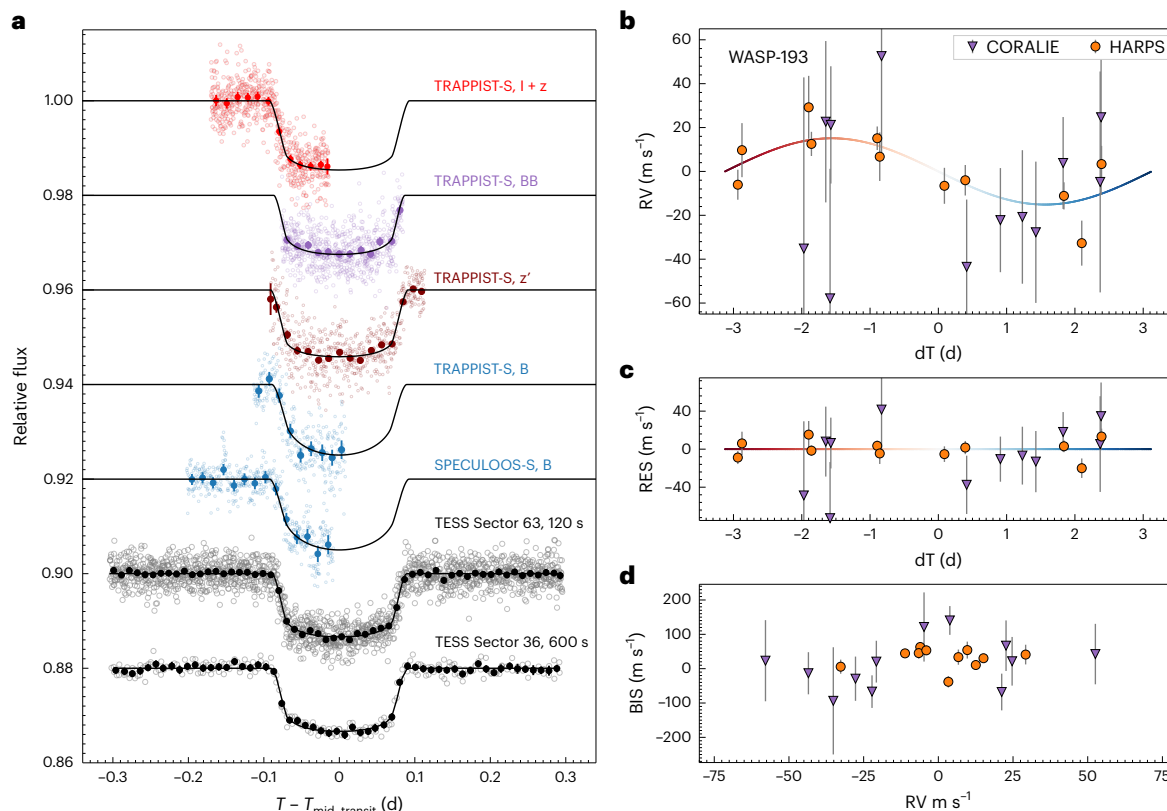
Fig. 1 | Photometric and spectroscopic follow-up. a, Follow-up transit photometry of WASP-193 b. Four transits were observed by TRAPPIST-South, one by SPECULOOS-South, and the observations performed by TESS in Sectors 36 and 63 with 10 min and 2 min cadences, respectively. In all the cases, the period-folded is shown using the best-fitting transit ephemeris deduced from our global MCMC analysis. Each transit light curve has been corrected by the baseline model presented in Supplementary Table 1. The coloured points with error bars are data binned to 20 min, and the best-fitting model is superimposed in black. The light curves are shifted by 0.02 along the y axis for clarity. **b**, RVs obtained with the CORALIE and HARPS spectrographs for WASP-193 period-folded using the best-fitting orbital model, which is superimposed as a solid line (in m s⁻¹). The RV colour line of the best fitting shows the Doppler effect. **c**, RV residuals of the fit (RES, in m s⁻¹). The coloured triangles and circles correspond to the CORALIE and the HARPS data, respectively. **d**, Bisector span as a function of RV (BIS, in m s⁻¹) of WASP-193 obtained with the CORALIE and HARPS spectrographs. We assumed that the bisector span error bars are twice the RV error bars[88]. dT and $T − T_{\text{mid-transit}}$ are times from the mid-transit.

fluxes corresponding to 600 s (Sector 36 in 2021) and 120 s (Sector 63 in 2023) (Methods). In addition, we used the Euler-1.2 m/CORALIE[5] and ESO-3.6 m/HARPS[6] spectrographs to observe WASP-193. We obtained 12 and 11 spectroscopic measurements with CORALIE and HARPS in 2015 and 2019, respectively (Methods).

All the follow-up data were consistent with the planetary origin of the transit signal identified by WASP. The high-precision follow-up light curves acquired in different filters showed no chromatic dependence (Fig. 1a). Indeed, the transit depths obtained with different bands agree at the 1σ level (Methods). The radial velocities (RVs) phased up with the transit time and period of 6.25 d, consistent with the transit timings, and the bisector analysis of the HARPS and CORALIE spectra[7] did not reveal any dependence of the measured radial velocities with the bisector span (Fig. 1b–d).

To constrain the stellar atmospheric parameters of WASP-193, we co-added HARPS and CORALIE spectra to produce a single stellar spectrum with a high signal-to-noise ratio (S/N ≈ 75) and analysed it as described in ref. 8. This analysis enabled us to constrain the following parameters: the spectral type, the metallicity [Fe/H], the effective temperature T_{eff}, the surface gravity log $g_\star$ and the rotational velocity $V\sin(i)$ (Methods). The resulting values show that WASP-193 is a F9-type Sun-like star with $T_{\text{eff}} = 6,076 \pm 120$ K, log $g_\star = 4.1 \pm 0.1$ dex, [Fe/H] = −0.06 ± 0.09 dex and $V\sin(i) = 4.3 \pm 0.8$ km s⁻¹. Using our measured T_{eff}, the star's magnitudes in different broadband filters and its Gaia Early Data Release 3 parallax[9], we conducted a spectral energy distribution (SED) fitting to derive a stellar radius of $R_\star = 1.225^{+0.032}_{-0.029} R_\odot$

using the EXOFASTv2[10] pipeline (Methods). Adopting T_{eff}, [Fe/H] and $R_\star$ as the basic input set, we then derived the stellar mass $M_\star$ and age $t_\star$ from stellar evolutionary modelling. We used the CLES code (Code Liégeois d'Évolution Stellaire[11]), building the best-fit stellar evolutionary track according to the input parameters following the Levenberg–Marquadt minimization scheme, as explained in ref. 12. We obtained $M_\star = 1.102 \pm 0.070 M_\odot$ and $t_\star = 4.43 \pm 1.92$ Gyr (Methods).

We derived the system's parameters by conducting a global model fitting together the photometric and spectroscopic data using the latest version of the Markov chain Monte Carlo (MCMC) code described in ref. 13, using the Mandel and Agol[14] and two-body Keplerian[15] models, respectively (Methods). Table 1 shows the deduced stellar and planetary physical parameters along with their 1σ intervals.

We find that planet has a radius of $R_p = 1.464 \pm 0.058 R_J$ and a mass of $M_p = 0.139 \pm 0.029 M_J$ (~3 M_{Neptune}), resulting in a surprisingly low density of $\rho_p = 0.059 \pm 0.014$ g cm⁻³ (Fig. 2a). This extremely low density positioned WASP-193 b as the second lightest planet discovered so far after Kepler-51 d ($\rho = 0.04 \pm 0.01$ g cm⁻³; both planets' densities connected at the 1σ level), and as the lightest planet over the hot-Jupiter population. It is worth noting that we restricted our comparison to planets that are precisely characterized, with dynamical masses and radii precisions better than 25% and 8%, respectively[16]. This approach aimed to eliminate any potential bias introduced by comparing WASP-193 b with inadequately characterized planets that could impede conclusive findings. Notably, these poorly characterized planets show a 1σ level association with distinct planet populations, further emphasizing

Table 1 | The WASP-193 system parameters derived from our global MCMC analysis (medians and 1σ limits of the marginalized posterior probability distributions)

Parameter	Symbol	Value (circular, e=0)	Value (eccentric, e≠0)	Unit
Deduced stellar parameters	**WASP-193**			
Mean density	$\rho_\star$	$0.567^{+0.051}_{-0.048}$	$0.557^{+0.051}_{-0.047}$	$\rho_\odot$
Stellar mass	$M_\star$	1.068 ± 0.066	$1.059^{+0.067}_{-0.068}$	$M_\odot$
Stellar radius	$R_\star$	1.235 ± 0.027	1.239 ± 0.028	$R_\odot$
Luminosity	$L_\star$	$1.87^{+0.18}_{-0.16}$	$1.88^{+0.18}_{-0.16}$	$L_\odot$
Deduced planet parameters	**WASP-193 b**			
Scaled semi-major axis	$a/R_\star$	11.81 ± 0.34	$11.74^{+0.35}_{-0.34}$	$R_\star$
Orbital semi-major axis	a	0.0678 ± 0.0014	0.0676 ± 0.0015	au
Orbital inclination	i_p	$88.51^{+0.57}_{-0.43}$	$88.49^{+0.78}_{-0.49}$	°
Eccentricity	e	0 (fixed)	$0.056^{+0.068}_{-0.040}$	–
Density	ρ_p	$0.059^{+0.015}_{-0.014}$	$0.059^{+0.015}_{-0.013}$	$g\,cm^{-3}$
Surface gravity	$\log g_p$	$2.23^{+0.09}_{-0.11}$	$2.22^{+0.09}_{-0.11}$	cgs
Mass	M_p	$0.141^{+0.029}_{-0.030}$	0.139 ± 0.029	M_J
Radius	R_p	$1.463^{+0.059}_{-0.057}$	$1.464^{+0.059}_{-0.057}$	R_J
Equilibrium temperature	T_{eq}	$1{,}252 \pm 30$	$1{,}254 \pm 31$	K
Irradiation	S_p	$5.58^{+0.57}_{-0.52} \times 10^5$	$5.62^{+0.53}_{-0.57} \times 10^5$	$W\,m^{-2}$

the challenge of performing a meaningful analysis of their nature due to significant degeneracies.

Remarkably, considering the irradiation of about $S_p = 6 \times 10^5\,W\,m^{-2}$ (or 440× larger than that of Earth) inferred from our analysis (Fig. 2b), classical evolution models of irradiated giant planets[17–20] are not able to reproduce the radius of WASP-193 b. Indeed, using the irradiated gas giant model from ref. 17 for a core mass of 0 to 10 $M_\oplus$ and age between 1.0 Gyr and 4.5 Gyr, the predicted radius is found to be 0.9–1.1 R_J. We also used the equation derived by ref. 19 from 35 exoplanets with $M_p < 150\,M_\oplus$. In this case, the resulting predicted radius is found to be $R_p = 0.82 \pm 0.14\,R_J$. Finally, we used the model of ref. 20 to calculate the radius of the planet using data from 286 hot Jupiters with known masses and radii. In this scenario, the predicted radius measures $R_p = 1.1 \pm 0.1\,R_J$. Therefore, WASP-193 b joins thus the subgroup of 'anomalously large' irradiated gas giants[21].

Planet interior

In the core accretion model, planets at this mass range are expected to have non-negligible amounts of heavy elements[22]. This is at odds with the low density of WASP-193 b. Alternatively, the planet could have formed by disk instability, as it was recently shown by ref. 23 that magnetically controlled disk fragmentation could lead to intermediate-mass clumps of H–He. The formation mechanism of planets like WASP-193 b remains uncertain, including its potential orbital evolution and we hope that future formation models can address its formation mechanism.

We calculated the evolution of WASP-193 b following the framework presented by ref. 24, which assumes a 'hot start' core accretion formation scenario[25]. The models use the equations of state[26] for H–He and for a 50:50 water–rock mix[27]. The planetary radius corresponds to the photosphere where the optical depth drops below two-thirds. Gas opacities are taken from ref. 28. Additional details on the interior evolution model can be found in ref. 24. We adapted the evolution models of ref. 24 to account for the evolution of the host star where the stellar luminosity follows a pre-calculated stellar evolution track. The luminosity as a function of time was calculated with the MESA Isochrones and Stellar Tracks (MIST)[29,30] with a mass of $M_\star = 1.068\,M_\odot$ and slightly subsolar metallicity

[Fe/H] = −0.06 obtained from our spectroscopic analysis. The age range of the planet was defined by the ages at which the stellar luminosity from the evolution tracks matched the inferred one $L = 1.87^{+0.18}_{-0.16}\,L_\odot$ (Methods). As there is no clear correlation between stellar metallicity and the composition of giant planets[31], the bulk composition of WASP-193 b cannot be inferred from the measured stellar [Fe/H]. As a result, we considered two end members of the planetary composition (that is, planetary metallicity). First, we calculated the evolution of WASP-193 b with metallicity $Z = 0.0$, representing the lowest metallicity case. Naively, one would expect a pure H–He planet to yield the largest radius (and lowest density) at a given time. However, as a metal-enriched atmosphere has a higher opacity and therefore delays the cooling, a planet with $Z > 0$ could actually contract more slowly[32]. It has been shown that a turn-over value of Z exists for which the effect of the increased density wins over the delayed cooling. After that, the planetary size decreases with increasing Z (see ref. 32 for further details). For planet WASP-193 b, the turn-over value is $Z = 0.1$. Therefore, we also considered the evolution of WASP-193 b with $Z = 0.1$. The evolution of the planetary radius for the two cases is shown in Fig. 3. While the enriched atmosphere in the $Z = 0.1$ case yielded a larger radius until around 1 Gyr, it is clear that neither model can reproduce the observed radius of WASP-193 b for the possible stellar ages. The influence of the stellar evolution is more profound at early times when the star has a higher luminosity. The planet cools down as the stellar luminosity decreases and the star reaches the main sequence. We find that the planet has a size comparable to that of WASP-193 b only for an age of a few 10 Myr, which is inconsistent with the estimated age of the host star. Clearly, the large observed radius of ~1.5 R_J at an age of several billion years cannot be reproduced unless other mechanisms are at work, these include processes that (1) delay the cooling of the planet, or (2) deposit heat deep in the planetary interior and mass loss, all of which are in principle dependent on metallicity Z. We discuss such mechanisms below.

Delay in planetary cooling
Inefficient cooling can be caused by various processes, such as an enhanced atmospheric opacity that leads to longer cooling timescales,
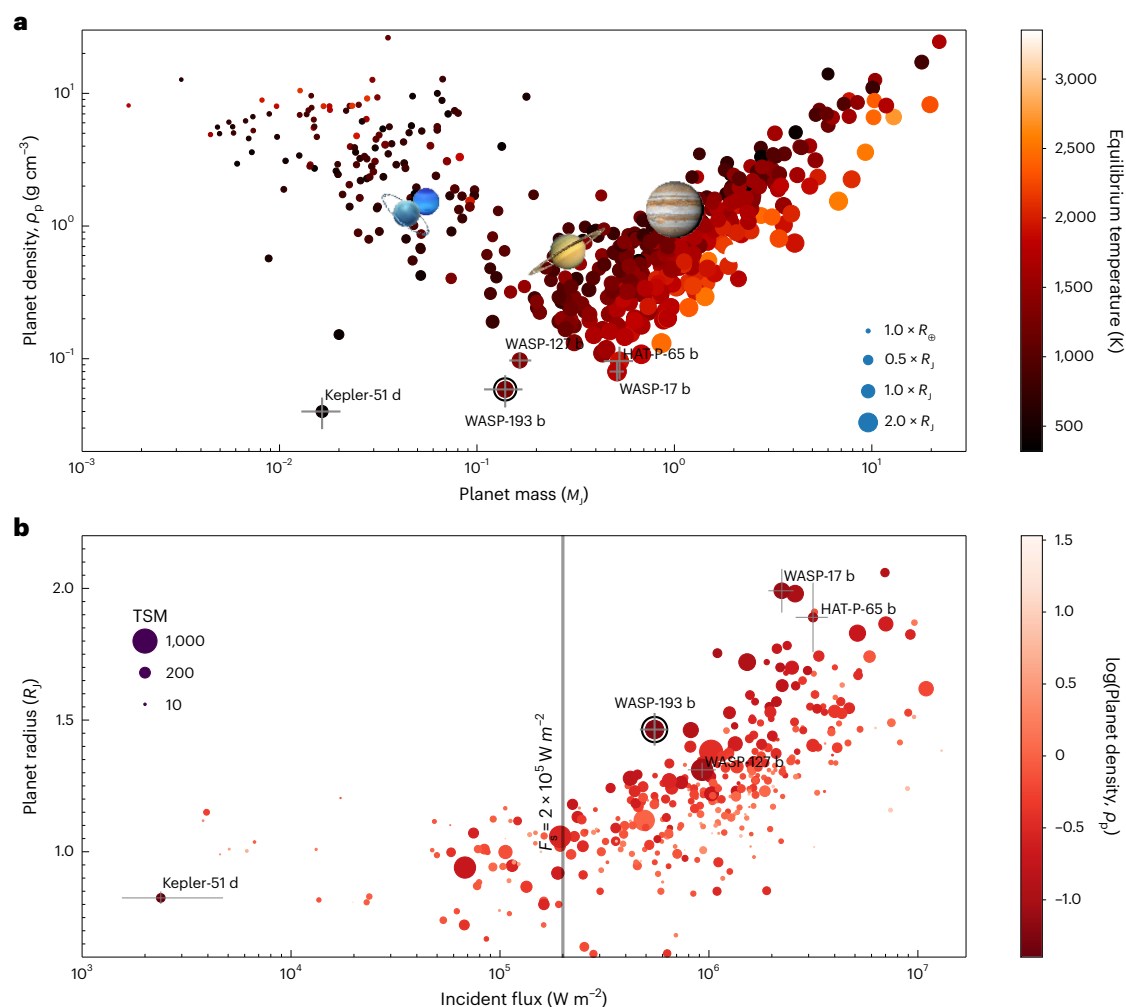
Fig. 2 | Planetary diagrams of known transiting exoplanets with radius and mass precisions better than 8% and 25%, respectively. a, Planetary density as a function of the planetary mass. The size of the points scale with the planetary radius. The points are coloured according to their equilibrium temperature. WASP-193 b and the least dense planets known so far are labelled and shown with their 1σ uncertainties (Kepler-51 d[89], WASP-17 b[90], WASP-127 b[91] and HAP-P-65 b[92]).

b, Planetary radius as a function of the stellar incident flux. The size of the points scale with the TSM[43]. The points are coloured according to their planetary density. The radii begin to show a correlation with stellar incident fluxes at $F_s \approx 2 \times 10^5$ W m^{-2} (vertical grey line)[93]. The planetary diagrams were obtained from the NASA Exoplanets Archive (https://exoplanetarchive.ipac.caltech.edu/).

interiors that are not fully convective and phase separations. For the former, as we show in Fig. 3, the effect of prolonged cooling via opacity enhancement is insufficient to explain the large radius of WASP-193 b. In addition, it is possible that the opacity is enhanced due to dust grains or cloud decks, which were not included in our models. However, it is unlikely that this would increase the radius beyond a few per cent[33]. Also, in the case of a not fully convective interior, the planet contracts at a lower rate. This can occur when the interior consists of boundary layers and/or composition gradients[34]. Such a configuration can lead to much higher internal temperatures at a given age[35] and is expected to lead to an increase in radius by up to ~10% (ref. 36). Therefore, this scenario also cannot explain the large observed radius. Phase separation could also lead to slower cooling. In giant planets, He rain can delay the planetary cooling[37]. Its ability to increase the planetary radii is, however, limited to a few per cent[38]. More importantly, a planet of ~0.14 M_J such as WASP-193 b is not expected to reach internal pressures that are high enough for He to become immiscible[38]. A self-consistent model that incorporates layered convection, tidal heating, boundary layers as well as enhanced opacities and dust-rich atmospheres to delay the cooling to its maximum would be required to fully evaluate whether the combined mechanisms are sufficient to explain the measured radius.

However, the observed radius of WASP-193 b is 40–50% larger than predictions from evolution models. Therefore, these mechanisms are unlikely to add up to account for the inflated radius fully.

Heat deposition and mass loss

The planet may be heated at depth due to ohmic dissipation or tidal heating. However, tidal heating is unlikely to be the mechanism that inflates hot Jupiters as it has been observed that the inflated radii correlate with stellar flux better than with the distance to the hot star[19,39]. Currently, ohmic dissipation seems to be the most promising mechanism[40]. This is because the atmosphere of WASP-193 b is sufficiently hot (equilibrium temperature $T_{eq} \approx 1,250$ K) that trace elements in the H–He gas can be partially ionized and allow for atmospheric currents to penetrate deep into the interior. For hot Jupiters, the radius inflation power depends on the incident flux[41]. If WASP-193 b experiences similar inflation mechanisms, this suggests that mechanisms that are coupled to stellar heating, including ohmic dissipation, are favourable, and possibly, multiple mechanisms are at play. Additional heating in the deep interior could be occurring together with semi-convective and/or boundary layers. This could effectively trap some of the deposited energy and delay the planetary cooling.

We estimate the additional energy required to explain the observed radius of WASP-193 b independent of the heating mechanism. We determine the planetary total internal energy E_0 at a time t_0 where the planet's radius matches the observed one. The energy required for the additional inflation is then $\Delta E = E_0 - E_{today}$, where E_{today} is the internal energy at the mean stellar age. We find that $t_0 = 40$ Myr ($Z = 0$) and $t_0 = 60$ Myr ($Z = 0.1$), which yielded a similar $\Delta E \approx 10^{40}$ erg for the two cases. For comparison, the energy WASP-193 b receives today by the stellar irradiation is ~5×10^{36} erg yr^{-1}, about four orders of magnitude lower.

Finally, the relatively low mass of WASP-193 b, its high stellar irradiation and its location at the edge of the sub-Jovian valley in the mass–radius diagram might hint that it may be losing mass. If this is the case, the extended observed radius may be related to material evaporating and leaving the planet. However, this is only a speculation, and we stress that there is no indication in the measurements for atmospheric loss. It is possible to use theoretical models of mass loss for highly irradiated planets to estimate whether atmospheric escape is important for WASP-193 b. We calculate the restricted Jeans escape parameter $\Lambda \propto M_p / T_{eq} R_p$ from ref. [42], which can be used to identify planets for which atmospheric escape is important. For WASP-193 b, we find $\Lambda = 3.7$. It was shown in ref. [42] that Λ values lower than the critical value of $\Lambda_T = 15-35$ correspond to notable atmospheric loss. As a result, the atmospheric mass loss could be important for WASP-193 b. However, we emphasize that detailed hydrodynamic simulations should be performed to fully assess the importance of atmospheric escape for WASP-193 b.

Overall, the evolution model cannot explain the observations of WASP-193 b, despite it being state of the art. A self-consistent model that incorporates layered convection, boundary layers, as well as enhanced opacities and dust-rich atmospheres to delay the cooling to its maximum would be required to evaluate whether the combined mechanisms are sufficient to explain the measured radius. However, this would require considerable effort in improving existing evolution models, which is outside the scope of this study. Besides advances in modelling, additional constraints on the atmospheric escape, composition and temperature structure might be obtained by conducting transit spectroscopy using the JWST, providing key information to unravel the nature of this low-density planet, as discussed in the following.

Atmospheric characterization prospects

Owing to its remarkably low density, the hot-Jupiter WASP-193 b is a prime target for atmospheric characterization. As highlighted in Fig. 4, its transmission spectroscopy metric (TSM)[43] is among the highest so far (~600). We used the TIERRA retrieval framework[44] to assess quantitatively the insights that would be accessible with a single visit of JWST. To this end, we performed an injection retrieval on a synthetic WASP-193 b atmosphere using abundances consistent with WASP-39 b (Methods). We assume the use of NIRSpec/Prism (near-infrared spectrograph) as its wavelength coverage provides the best trade-off for atmospheric exploration. The synthetic data, the best fit and the retrieved planetary parameters are shown in Fig. 5. We find that a single transit observation can yield the abundances of strong absorbers within 0.1 dex, assuming no remarkable opacity challenge[44] as expected for hot Jupiters[45]. Most importantly, we find that the planetary mass is tightly constrained within ~1% compared with the current ~20% precision achieved with radial velocity measurements. This tight constraint is enabled by the independent constraints on the atmospheric scale height ($H = 3,008 \pm 119$ km), temperature and abundance accessible via transmission spectroscopy at such high TSM[46]. While a single visit with JWST/NIRSpec/Prism would provide the most insights into the planetary atmosphere, a single JWST/NIRISS (near-infrared imager and slitless spectrograph)/SOSS (single object slitless spectroscopy) observation would also allow to detect the He absorption triplet, and this would provide preliminary insights into the current atmospheric loss[47]. Ground-based high-resolution measures could later
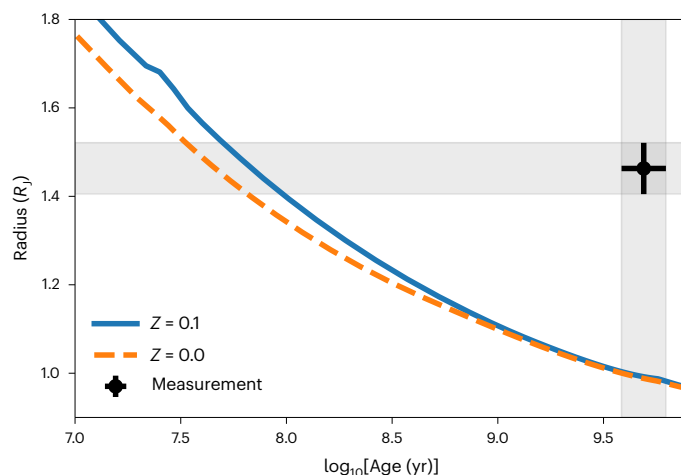

Fig. 3 | Planetary radius as a function of age for two evolution models. The orange dashed line and solid blue lines are for $Z = 0.0$ and $Z = 0.1$, respectively, where Z is the planetary metallicity. The radius and age inferred from observations are shown as the black error bars and the grey-shaded regions. The radius evolution of the planet includes the effect of the evolving stellar irradiation (see text for details). Note that the slow cooling of the model with $Z = 0.1$ allows for larger radii compared with a pure H–He composition.

complement this picture by constraining the line profile[48], helping to validate or dismiss the hypothesis that atmospheric loss is responsible for the observed low-density nature of this planet. Moreover, using the NIRISS/SOSS, it would also be possible to place some constraints on the atmospheric metallicity (M/H), carbon-to-oxygen ratio (C/O) and potassium-to-oxygen ratio (K/O)[49], shedding some light on the formation process of WASP-193 b. For example, the hypothetical combination of a supersolar metallicity, supersolar K/O ratio and subsolar C/O ratio may suggest that the planet formed beyond the H$_2$O snow line followed by inwards migration, producing an efficient accretion of planetesimals[50]. Therefore, in general terms, the characteristics of WASP-193 b, along with its exquisite suitability for atmospheric characterization, position it as a benchmark planet for gaining insights into the properties of the population of low-density planets.

Methods

WASP observations and data reduction

The Super-WASP (Wide Angle Search for Planets)[1] project consists of data obtained at telescopes located at two sites: Sutherland Station of the South African Astronomical Observatory (SAAO) and the Observatorio del Roque de los Muchachos on the island of La Palma in the Canary Islands. The field of view (FOV) of each instrument is 482 deg^2 with a pixel scale of 13.7′ pixel^{-1}. These instruments are capable of obtaining photometry with a precision better than 1% for objects with V magnitudes between 7.0 and 11.5 (ref. [1]). The WASP ground-based transit survey has discovered almost 200 planets, transiting bright nearby stars, mostly hot Jupiters plus minor fraction of short-period Saturn- and Neptune-mass objects. Many WASP planets have proven to be among the most favourable targets for detailed atmospheric characterization with current facilities such as the HST[51], VLT[52], Magellan[53] and JWST[54] (for example, WASP-17 b[55], WASP-101 b[56], WASP-121 b[57] and WASP-127 b[58]).

The host star WASP-193 was observed by the WASP-South survey in 2006 and 2012. The WASP data calibration (bias and dark subtraction, and flat-field division) was performed using a bespoke pipeline[59] developed in Fortran. Aperture photometry was performed on the final calibrated images, where the stars' fluxes were measured in three photometric apertures with radii of 2.5, 3.5 and 4.5 pixels, following the method described by refs. [1,59,60]. The WASP phase-folded light
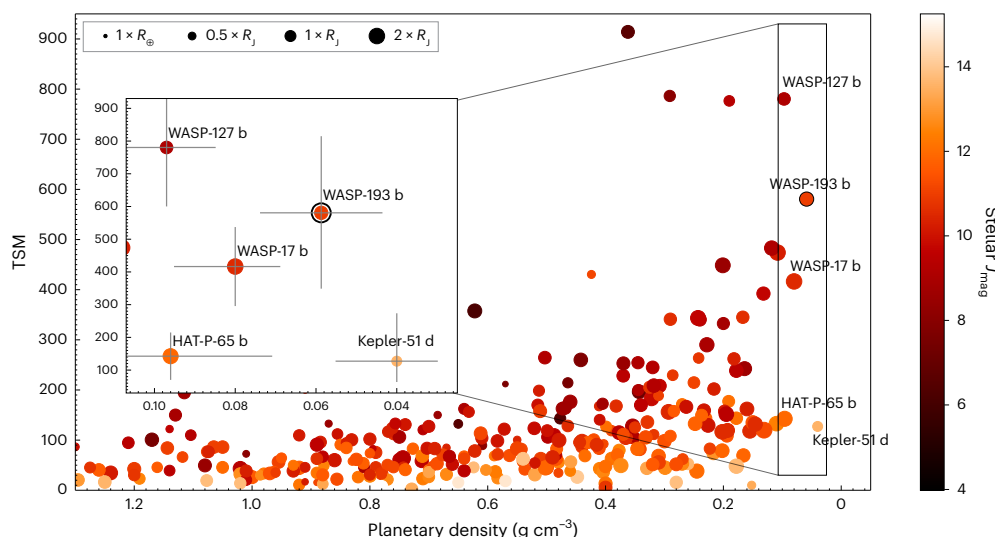
Fig. 4 | Feasibility of WASP-193 b for transmission spectroscopy studies.
The TSM is presented as a function of the planetary density of known transiting exoplanets obtained from the NASA Exoplanet Archive (https://exoplanetarchive.ipac.caltech.edu/) with radius and mass precisions better than 8% and 25%, respectively. The point size scales with the planetary radius. The points are coloured according to the host star 2MASS J-magnitude. WASP-193 b is highlighted with a black contour.

curve obtained for WASP-193 is presented in Supplementary Fig. 1. The search for transit events in the WASP photometry was conducted using the box-least-square method as described in ref. 59. The alert for this candidate triggered the ground-based follow-up campaign using both photometry and spectroscopy measurements to confirm the planetary nature of the detected signal.

TRAPPIST-South photometry

The TRAPPIST (Transiting Planets and PlanetesImals Small Telescope) network is composed of the 0.6 m twin robotic telescopes TRAPPIST-South and TRAPPIST-North[2,61,62]. For WASP-193, we used TRAPPIST-South located at the La Silla observatory in Chile. It is equipped with a thermo-electrically 2K × 2K FLI ProLine PL3041-BB charge-coupled device (CCD) camera with a FOV of 22′ × 22′ and a pixel scale of 0.65″ per pixel. TRAPPIST-South observed a full transit of WASP-193 b in the Sloan-z′ filter on 27 January 2017 with an exposure time of 20 s, and three partial transits, one in the I + z filter on 02 January 2015 with an exposure time of 10 s, one in the BB filter on 06 April 2015 with an exposure time of 8 s, and a last one in the Johnson-B filter on 08 June 2019 with an exposure time of 25 s. Data calibration and differential photometry were performed using the PROSE pipeline[63]. The reduced light curves obtained for WASP-193 b along with the best-fitting model are presented in Fig. 1 and Supplementary Table 1.

SPECULOOS-South photometry

The SPECULOOS (Search for Habitable Planets Eclipsing Ultra-cool Stars) robotic telescope network is composed of the SPECULOOS Southern Observatory[3,64,65] (SSO), with four 1 m telescopes at ESO Paranal Observatory in Chile and two 1 m telescopes in the Northern Hemisphere: the SPECULOOS Northern Observatory[66] (SNO) at Teide Observatory in Spain and SAINT-EX[67] (Search and Characterisation of Transiting Exoplanets) at San Pedro Mártir Observatory in Mexico. These facilities are identical Ritchey–Chretien telescopes equipped with ANDOR iKon-L BEX2-DD cameras and 2,048 × 2,088 e2v CCD detectors, with a FOV of 12′ × 12′ and a pixel scale of 0.35″ per pixel. We observed a partial transit of WASP-193 b with one of the four telescopes of SSO on 08 June 2019 in the Johnson-B filter with an exposure time of 25 s. Data calibration and differential photometry were performed using the PROSE pipeline[63]. The reduced light curve obtained jointly with the best-fitting model is presented in Fig. 1 and Supplementary Table 1.

TESS photometry

The TESS (Transiting Exoplanet Survey Satellite)[4] mission was launched by NASA in April 2018. Its main goal is to detect and characterize transiting exoplanets smaller than Neptune orbiting nearby bright stars. TESS's combined FOV is 24° × 96°, and one pixel is ~21′ on the sky. WASP-193 was observed by TESS with a 30 min cadence in the ninth sector of its primary mission (from 28 February to 26 March 2019), with a 10 min cadence during its extended mission in Sector 36 (from 07 March to 02 April 2021) and with 2 min cadence in Sector 63 (from 10 March 2023 to 06 April 2023). We retrieved the light curves produced by the TESS Science Processing Operations Center pipeline[68–70] (PDC-SAP) corresponding to the 2 min and 10 min cadences from the Mikulski Archive for Space Telescope. These light curves are corrected for instrument systematics and crowding effects. TESS light curves corresponding to the 2 min and 10 min cadences for WASP-193 b and the best-fitting model are presented in Fig. 1 and Supplementary Table 1.

Spectroscopic and RV measurements

In this paper, we used RV measurements obtained by CORALIE (mounted on the 1.2 m Swiss Euler telescope located at ESO La Silla in Chile[5]) and HARPS (mounted on the 3.6 m telescope at ESO La Silla in Chile[6]) spectrographs. We obtained 12 (between June 2015 and June 2018) and 11 (between February and July 2019) spectroscopic measurements of WASP-193 with the CORALIE and HARPS spectrographs, respectively. We applied the cross-correlation method[71] on the observed spectra of WASP-193 to extract the RV measurements.

The RV measurements of WASP-193 are in phase with the ephemerides from the WASP-South photometric data, but the planet was not independently detected in the RV data. The offset between RV datasets is taken into account by modelling the systematic velocity for each instrument during the global analysis. The marginally strongest signal in the generalized Lomb–Scargle periodogram[72] coincided with the transit period of 6.25 d, although the significance was below 10% false alarm probability (FAP). The RV measurements obtained with CORALIE and HARPS are presented in Supplementary Table 2 and the phase-folded RV curve of WASP-193 is presented in Fig. 1. The corresponding RV based on the fitting linear slope enables us to discard the blended eclipsing binary scenario and to keep the planetary companion hypothesis. The correlation between the bisector spans and RVs is shown in Fig. 1d, which was consistent with zero, that is, there is
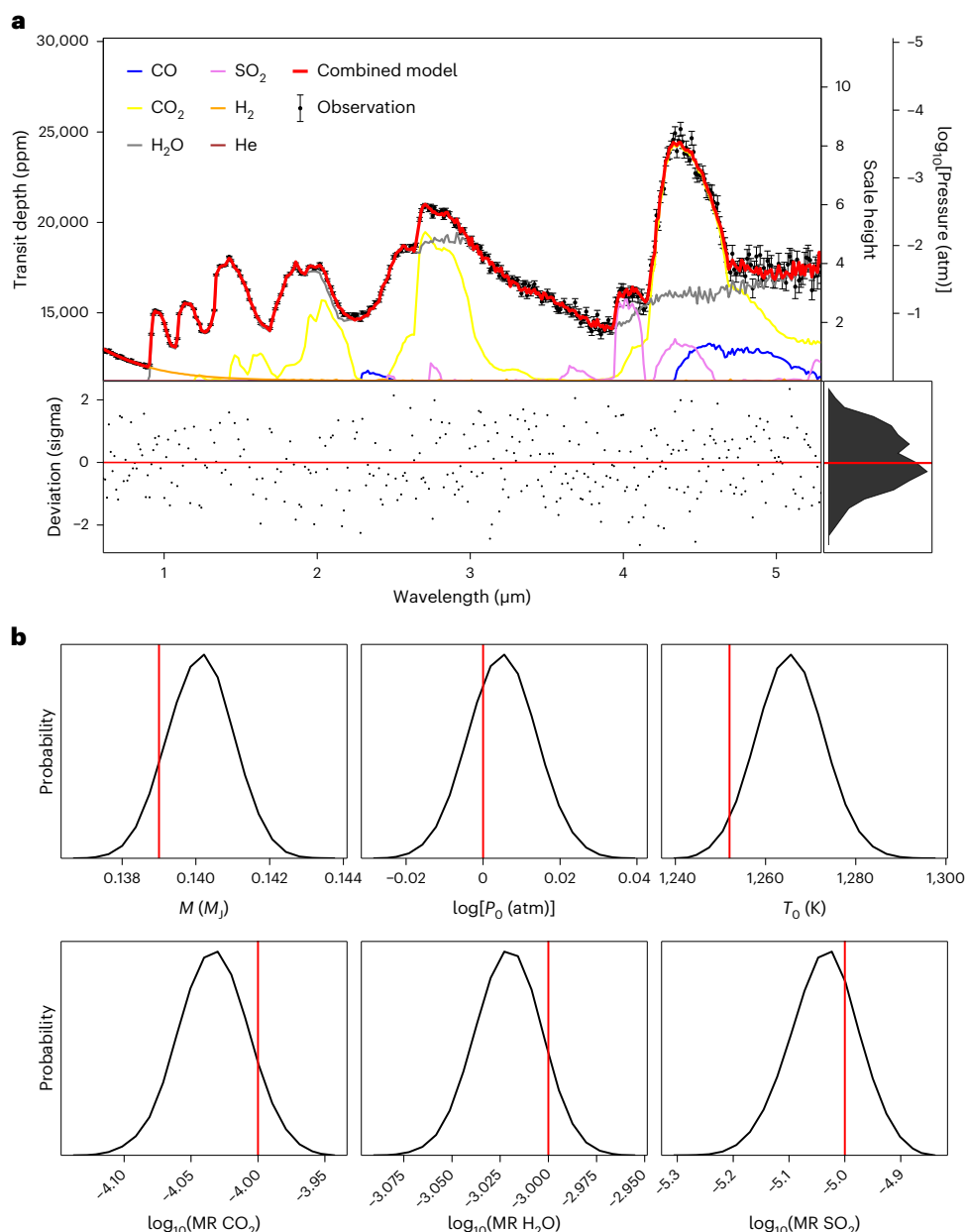
Fig. 5 | WASP-193 b as an exquisite target for atmospheric characterization.
a, Synthetic transmission spectrum model and best-fit model for the injection-retrieval test for a single JWST/NIRSpec/Prism transit of WASP-193 b. Models and tests are produced with the TIERRA pipeline[44]. **b**, Posterior probability distributions of the key planetary properties retrieved, showcasing that one single JWST visit can yield the constraints on the main atmospheric properties and the planetary mass within ~0.1 dex and ~1%, respectively. The red line represents the true value used in generating the synthetic spectrum. MR is the volume mixing ratio and P_0 is the reference pressure corresponding to reference radius.

no remarkable correlation between these two parameters. Moreover, we calculated the Pearson r coefficient to measure the correlation between these two parameters, and we obtained $r_{Harps} = 0.07$ for HARPS and $r_{Coralie} = 0.21$ for CORALIE. Therefore, the Pearson r coefficient confirmed no significant correlation between the bisector spans and RVs, supporting the planetary nature of WASP-193 b.

We used co-added spectra obtained with the HARPS spectrograph to produce a single spectrum with an S/N of 75, which allowed us to constrain the stellar atmospheric parameters of WASP-193 better using the method described by ref. 8. The metallicity, [Fe/H], was computed from the Fe lines, the effective temperature, T_{eff}, was computed from the Hα line, the surface gravity, log g, was estimated from the Mg Ib and Na ID lines, the activity index, $log(R'_{hk})$, was constrained from the Ca II H + K lines and the rotational velocity, $V\sin(i)$, was measured by assuming a macroturbulence value of $v_{macro} = 4.45$ km s^{-1}, which was

extracted from the calibration formula[73], and a microturbulence value of $v_{micro} = 1.17$ km s^{-1}, which was extracted from the calibration formula[74]. With these values, it was found that WASP-193 is a Sun-like star with $T_{eff} = 6,076 \pm 120$ K, $\log g_\star = 4.1 \pm 0.1$ dex, [Fe/H] = -0.06 ± 0.09 dex, $V\sin(i) = 4.3 \pm 0.8$ km s^{-1} and $\log(R'_{hk}) = 5.30 \pm 0.07$ dex. Using the MKCLASS program[75], we obtained a spectral type of F9 from the observed HARPS spectrum. This is consistent with that estimated from the stellar atmospheric parameters and $B - V$ colour index.

Stellar parameters from the ExoFASTv2 analysis

As an independent check of the derived stellar parameters for WASP-193, we performed an analysis using the exoplanet fitting suite, EXO-FASTv2 (refs. 10,76). EXOFASTv2 uses a differential evolution MCMC to globally and simultaneously model the star and planet. The built-in Gelman–Rubin statistic[77,78] is used to check the convergence of the

chains. A full description of EXOFASTv2 is given in ref. 10. Within the fit, the host star's parameters are determined using the SEDs (Supplementary Fig. 2) constructed from our broadband photometry, MIST evolutionary models[29,30]. For the SED fits performed within EXOFASTv2, we used photometry from APASS DR9 BV[79], 2MASS HK[80], and ALL-WISE W1, W2 and W3 (ref. 81), which are presented in Supplementary Table 3.

We applied Gaussian priors to the parameters T_{eff}, $\log g_\star$ and [Fe/H] using the obtained values from the spectroscopic analysis. We also enforced Gaussian priors on the Gaia Data Release 3 (ref. 9) parallax (adding 82 µas to the reported value and adding 33 µas in quadrature to the error, following the recommendation of ref. 82). We adopted an upper limit on the extinction of $A_V = 0.20$ from ref. 83. The EXOFASTv2 fit results are presented in Supplementary Table 3.

Stellar parameters using CLES

We used our Liège stellar evolution code, CLES, to determine the age and mass of the host star. All the details concerning the input physics (treatment of convection, surface boundary conditions, nuclear reaction rates, equation of state, opacities and diffusion) can be found in section 2.3 of ref. 12. We adopted the solar mixture of ref. 84. As inputs, we used the spectroscopic T_{eff} and [Fe/H], as well as the stellar radius $R_\star$ obtained from SED-fitting using ExoFASTv2. We computed stellar evolutionary tracks and selected the best-fit one according to the input parameters following the Levenberg–Marquadt minimization scheme, as explained in ref. 12. We obtained $M_\star = 1.102 \pm 0.070\,M_\odot$ and $t_\star = 4.4 \pm 1.9$ Gyr (Supplementary Table 3).

Modelling of the spectroscopic and photometric data

We combined the spectroscopic and photometric observations of WASP-193 to determine the physical parameters of the planetary system. The stellar atmospheric parameters, T_{eff}, $\log g_\star$ and [Fe/H] from our spectroscopic analysis, were coupled with the stellar radius, $R_\star$, obtained using EXOFASTv2 and the mass, $M_\star$, obtained using CLES to infer the stellar density, $\rho_\star$, luminosity, $L_\star$, and other physical parameters.

We used an MCMC algorithm[13] to sample the posterior probability distributions of the system's parameters, from which we extracted the median values and their 1σ uncertainties. All photometric measurements contain additional faint ($G_{mag} \approx 16$) neighbour star at 4.2′ (Supplementary Fig. 3). The resulting dilution was found to be <5%, which is included in our global analysis.

We modelled the RV curves using a two-body Keplerian model[15], and the transit light curves using the Mandel and Agol[14] model multiplied by a baseline to correct for several external effects related to time, full-width at half-maximum, air mass, star position in the CCD, x and y, and background (Supplementary Table 1). The baseline model for each transit light curve was selected based on minimizing the Bayesian information criterion (BIC)[85] using the formula:

$$BIC = \chi^2 + k\log(N), \qquad (1)$$

where k is the number of free parameters, N is the number of data points, and $\chi^2 = -2\log(L)$, where L is the maximized value of the model's likelihood function. The light curve observed on 06 April 2015 with TRAPPIST-South contains a meridian flip (that is, a 180° rotation that the German equatorial mount has to undergo when the target star passes the local meridian) at BJD = 2,457,119.619198 (see details in Supplementary Table 1), that we modelled as a flux offset in our MCMC analysis.

The jump parameters in our MCMC analysis (that is, parameters randomly perturbed at each step of the MCMC; Supplementary Table 4) were:

- T_0: the transit timing
- W: the total duration of the transit (that is, the duration between ingress and egress)

- dF $= R_p^2/R_\star^2$: the transit depth, where R_p and $R_\star$ are the planetary and stellar radii, respectively
- $b' = a\cos(i)/R_\star$: the impact parameter, where i is the orbital inclination and a is the orbital semi-major axis
- P: the orbital period
- $K_2 = KP^{1/3}\sqrt{1-e^2}$, where K is the semi-amplitude of the RV and e is the orbital eccentricity
- $\sqrt{e}\cos(w)$ and $\sqrt{e}\sin(w)$, where w is the argument of periastron

The stellar parameters T_{eff}, [Fe/H] and $M_\star$ were also jump parameters in our analysis. For T_{eff}, [Fe/H] and $\log g_\star$, we applied Gaussian priors based on the results of our spectroscopic analysis.

We assumed a quadratic limb-darkening law to take into account the impact of limb darkening on our transit light curves. For each filter, the quadratic limb-darkening coefficients, u_1 and u_2, were interpolated from the tables of ref. 86 using the T_{eff}, $\log g_\star$ and [Fe/H] obtained from our spectroscopic analysis. For the non-standard I + z and BB filters, we took the averages of the values for the standard filters Ic and Sloan-z′ for the I + z filter, and Ic and Johnson-R for the BB filter. The limb-darkening coefficient values of u_1 and u_2 for each filter are presented in Supplementary Table 5.

We performed two independent MCMC analyses: one assuming a circular orbit (model 1) and the other assuming an eccentric orbit (model 2). For each model, we calculated the BIC value, which was then used to compute the Bayes factor (BF) using the relationship described by ref. 87. The Bayes factor (BF_{12}) was determined as $BF_{12} = e^{(BIC_{model2} - BIC_{model1})/2}$. Our analysis yielded a BF_{12} value of 20.1, indicating strong evidence in favour of the eccentric scenario[87].

For each transit light curve, a preliminary MCMC analysis composed of one Markov chain of 100,000 steps was performed to estimate the correction factor (CF) to rescale the photometric errors by $CF = \beta_{red} \times \beta_{white}$, where β_{red} is the red noise and β_{white} is the white noise, as described by ref. 13. For the RVs, a jitter noise (that is, the quadratic difference between the mean error of the measurements and the standard deviation of the best-fitting residuals) of 22.3 m s^{-1} for CORALIE and 4.1 m s^{-1} for HARPS was added quadratically to the RV error bars. Then, we conducted a global MCMC analysis composed of 5 chains of 100,000 steps. The convergence of each chain was checked using the statistical test presented by ref. 77. The transit depths derived for different photometric bands are consistent at the 1σ level, highlighting the non-chromatic dependence and supporting our planetary interpretation (Supplementary Table 4). The deduced parameters of the WASP-193 system are presented in Table 1. The stellar and planetary physical parameters posterior probability distributions are shown in Supplementary Figs. 4 and 5, respectively.

Atmospheric model and injection-retrieval test

The atmospheric model and the injection-retrieval test performed to assess the suitability of WASP-193 b for atmospheric exploration with JWST uses the TIERRA retrieval framework[44]. We model a synthetic WASP-193 b atmosphere using abundances consistent with WASP-39 b (volume mixing ratio of: CO, 10^{-5}; CO_2, 10^{-4}; H_2O, 10^{-3}; SO_2, 10^{-5}). We tested four different instrumental settings (NIRSpec Prism, NIRISS SOSS, NIRCAM F322W2 and NIRSpec G395H) and found that while all lead constraints on the planetary properties, JWST/NIRSpec Prism provides the most comprehensive constraints owing to its more extensive wavelength coverage. Figure 5 presents the synthetic data, the best fit and the retrieved planetary parameters.

Data availability

The TRAPPIST-South and SPECULOOS-South data analysed are available at CDS via anonymous ftp at http://cdsarc.u-strasbg.fr/ (130.79.128.5). The HARPS and CORALIE data analysed are available in the European Southern Observatory archive (ESO; http://archive.eso.org/cms.html) The TESS data analysed are available in the Mikulski

Archive for Space Telescopes (MAST; https://archive.stsci.edu/). Source data are provided with this paper.

Code availability

The Prose and MCMC codes used for this paper are publicly available.

References

1. Pollacco, D. L. et al. The WASP project and the SuperWASP cameras. *Publ. Astron. Soc. Pac.* **118**, 1407–1418 (2006).
2. Gillon, M. et al. TRAPPIST: a robotic telescope dedicated to the study of planetary systems. *EPJ Web Conf* **11**, 06002 (2011).
3. Jehin, E. et al. The SPECULOOS Southern Observatory begins its hunt for rocky planets. *The Messenger* **174**, 2–7 (2018).
4. Ricker, G. R. et al. Transiting Exoplanet Survey Satellite (TESS). *J. Astron. Telesc. Instrum. Syst.* **1**, 014003 (2015).
5. Queloz, D. et al. Extrasolar planets in the Southern Hemisphere: the CORALIE survey. In *From Extrasolar Planets to Cosmology: The VLT Opening Symposium* (eds Bergeron, J. & Renzini, A.) 548–555 (Springer, 2000).
6. Mayor, M. et al. Setting new standards with HARPS. *The Messenger* **114**, 20–24 (2003).
7. Torres, G., Konacki, M., Sasselov, D. D. & Jha, S. Testing blend scenarios for extrasolar transiting planet candidates. I. OGLE-TR-33: a false positive. *Astrophys. J.* **614**, 979–989 (2004).
8. Doyle, A. P. et al. Accurate spectroscopic parameters of WASP planet host stars. *Mon. Not. R. Astron. Soc.* **428**, 3164–3172 (2013).
9. Gaia Collaboration. VizieR Online Data Catalog: Gaia EDR3 (Gaia Collaboration, 2020). *VizieR Online Data Catalog* https://ui.adsabs.harvard.edu/abs/2020yCat.1350....0G (2020).
10. Eastman, J. D. et al. EXOFASTv2: a public, generalized, publication-quality exoplanet modeling code. Preprint at https://arxiv.org/abs/1907.09480 (2019).
11. Scuflaire, R. et al. CLÉS, Code Liégeois d'Évolution Stellaire. *Astrophys. Space Sci.* **316**, 83–91 (2008).
12. Salmon, S. J. A. J., Van Grootel, V., Buldgen, G., Dupret, M. A. & Eggenberger, P. Reinvestigating α Centauri AB in light of asteroseismic forward and inverse methods. *Astron. Astrophys.* **646**, A7 (2021).
13. Gillon, M. et al. The TRAPPIST survey of southern transiting planets. I. Thirty eclipses of the ultra-short period planet WASP-43 b. *Astron. Astrophys.* **542**, A4 (2012).
14. Mandel, K. & Agol, E. Analytic light curves for planetary transit searches. *Astrophys. J. Lett.* **580**, L171–L175 (2002).
15. Murray, C. D. & Correia, A. C. M. in *Exoplanets* (ed. Seager, S.) 15–23 (Univ. Arizona Press, 2010).
16. Luque, R. & Pallé, E. Density, not radius, separates rocky and water-rich small planets orbiting M dwarf stars. *Science* **377**, 1211–1214 (2022).
17. Fortney, J. J., Marley, M. S. & Barnes, J. W. Planetary radii across five orders of magnitude in mass and stellar insolation: application to transits. *Astrophys. J.* **659**, 1661–1672 (2007).
18. Baraffe, I., Chabrier, G. & Barman, T. Structure and evolution of super-Earth to super-Jupiter exoplanets. I. Heavy element enrichment in the interior. *Astron. Astrophys.* **482**, 315–332 (2008).
19. Weiss, L. M. et al. The mass of KOI-94d and a relation for planet radius, mass, and incident flux. *Astrophys. J.* **768**, 14 (2013).
20. Sestovic, M., Demory, B.-O. & Queloz, D. Investigating hot-Jupiter inflated radii with hierarchical Bayesian modelling. *Astron. Astrophys.* **616**, A76 (2018).
21. Lopez, E. D. & Fortney, J. J. Re-inflated warm Jupiters around red giants. *Astrophys. J.* **818**, 4 (2016).
22. Helled, R. et al. in *Protostars and Planets VI* (eds Beuther, H. et al.) 665 (Univ. Arizona Press, 2014).
23. Deng, H., Mayer, L. & Helled, R. Formation of intermediate-mass planets via magnetically controlled disk fragmentation. *Nat. Astron.* **5**, 440–444 (2021).
24. Müller, S. & Helled, R. Synthetic evolution tracks of giant planets. *Mon. Not. R. Astron. Soc.* **507**, 2094–2102 (2021).
25. Marley, M. S., Fortney, J. J., Hubickyj, O., Bodenheimer, P. & Lissauer, J. J. On the luminosity of young Jupiters. *Astrophys. J.* **655**, 541–549 (2007).
26. Chabrier, G., Mazevet, S. & Soubiran, F. A new equation of state for dense hydrogen–helium mixtures. *Astrophys. J.* **872**, 51 (2019).
27. More, R., Warren, K., Young, D. & Zimmerman, G. A new quotidian equation of state (QEOS) for hot dense matter. *Phys. Fluids* **31**, 3059–3078 (1988).
28. Freedman, R. S. et al. Gaseous mean opacities for giant planet and ultracool dwarf atmospheres over a range of metallicities and temperatures. *Astrophys. J. Suppl. Ser.* **214**, 25 (2014).
29. Choi, J. et al. Mesa Isochrones and Stellar Tracks (MIST). I. Solar-scaled models. *Astrophys. J.* **823**, 102 (2016).
30. Dotter, A. MESA Isochrones and Stellar Tracks (MIST) 0: methods for the construction of stellar isochrones. *Astrophys. J. Suppl. Ser.* **222**, 8 (2016).
31. Teske, J. K., Thorngren, D., Fortney, J. J., Hinkel, N. & Brewer, J. M. Do metal-rich stars make metal-rich planets? New insights on giant planet formation from host star abundances. *Astron. J.* **158**, 239 (2019).
32. Müller, S., Helled, R. & Cumming, A. The challenge of forming a fuzzy core in Jupiter. *Astron. Astrophys.* **638**, A121 (2020).
33. Poser, A. J., Nettelmann, N. & Redmer, R. The effect of clouds as an additional opacity source on the inferred metallicity of giant exoplanets. *Atmosphere* **10**, 664 (2019).
34. Vazan, A., Helled, R. & Guillot, T. Jupiter's evolution with primordial composition gradients. *Astron. Astrophys.* **610**, L14 (2018).
35. Leconte, J. & Chabrier, G. A new vision of giant planet interiors: impact of double diffusive convection. *Astron. Astrophys.* **540**, A20 (2012).
36. Kurokawa, H. & Inutsuka, S.-i On the radius anomaly of hot jupiters: reexamination of the possibility and impact of layered convection. *Astrophys. J.* **815**, 78 (2015).
37. Stevenson, D. & Salpeter, E. The dynamics and helium distribution in hydrogen-helium fluid planets. *Astrophys. J. Suppl. Ser.* **35**, 239–261 (1977).
38. Fortney, J. J. & Hubbard, W. Effects of helium phase separation on the evolution of extrasolar giant planets. *Astrophys. J.* **608**, 1039 (2004).
39. Laughlin, G., Crismani, M. & Adams, F. C. On the anomalous radii of the transiting extrasolar planets. *Astrophys. J. Lett.* **729**, L7 (2011).
40. Fortney, J. J., Dawson, R. I. & Komacek, T. D. Hot jupiters: origins, structure, atmospheres. *J. Geophys. Res. Planets* **126**, e2020JE006629 (2021).
41. Thorngren, D. P. & Fortney, J. J. Bayesian analysis of hot-Jupiter radius anomalies: evidence for ohmic dissipation? *Astron. J.* **155**, 214 (2018).
42. Fossati, L. et al. Aeronomical constraints to the minimum mass and maximum radius of hot low-mass planets. *Astron. Astrophys.* **598**, A90 (2017).
43. Kempton, E. M. R. et al. A framework for prioritizing the TESS planetary candidates most amenable to atmospheric characterization. *Publ. Astron. Soc. Pac.* **130**, 114401 (2018).
44. Niraula, P. et al. The impending opacity challenge in exoplanet atmospheric characterization. *Nat. Astron.* **6**, 1287–1295 (2022).
45. Niraula, P., de Wit, J., Gordon, I. E., Hargreaves, R. J. & Sousa-Silva, C. Origin and extent of the opacity challenge for atmospheric retrievals of WASP-39 b. *Astrophys. J. Lett.* **950**, L17 (2023).
46. de Wit, J. & Seager, S. Constraining exoplanet mass from transmission spectroscopy. *Science* **342**, 1473–1477 (2013).
47. Seager, S. & Sasselov, D. D. Theoretical transmission spectra during extrasolar giant planet transits. *Astrophys. J.* **537**, 916–921 (2000).

48. Allart, R. et al. Spectrally resolved helium absorption from the extended atmosphere of a warm Neptune-mass exoplanet. *Science* **362**, 1384–1387 (2018).

49. Feinstein, A. D. et al. Early release science of the exoplanet WASP-39b with JWST NIRISS. *Nature* **614**, 670–675 (2023).

50. Mordasini, C., van Boekel, R., Mollière, P., Henning, T. & Benneke, B. The imprint of exoplanet formation history on observable present-day spectra of hot Jupiters. *Astrophys. J.* **832**, 41 (2016).

51. Meylan, G., Madrid, J. P. & Macchetto, D. Hubble Space Telescope science metrics. *Publ. Astron. Soc. Pac.* **116**, 790–796 (2004).

52. Pepe, F. A. et al. in *Ground-based and Airborne Instrumentation for Astronomy III* Vol. 7735 (eds McLean, I. S. et al.) 209–217 (SPIE, 2010).

53. Dressler, A. et al. IMACS: the Inamori-Magellan Areal Camera and Spectrograph on Magellan-Baade. *Publ. Astron. Soc. Pac.* **123**, 288–332 (2011).

54. Gardner, J. P. et al. The James Webb Space Telescope. *Space Sci. Rev.* **123**, 485–606 (2006).

55. Sing, D. K. et al. A continuum from clear to cloudy hot-Jupiter exoplanets without primordial water depletion. *Nature* **529**, 59–62 (2016).

56. Wakeford, H. R. et al. HST PanCET program: a cloudy atmosphere for the promising JWST target WASP-101b. *Astrophys. J.* **835**, L12 (2017).

57. Sing, D. K. et al. The Hubble Space Telescope PanCET program: exospheric Mg II and Fe II in the near-ultraviolet transmission spectrum of WASP-121b using jitter decorrelation. *Astron. J.* **158**, 91 (2019).

58. Skaf, N. et al. ARES. II. Characterizing the hot jupiters WASP-127 b, WASP-79 b, and WASP-62b with the Hubble Space Telescope. *Astron. J.* **160**, 109 (2020).

59. Collier Cameron, A. et al. A fast hybrid algorithm for exoplanetary transit searches. *Mon. Not. R. Astron. Soc.* **373**, 799–810 (2006).

60. Street, R. A. et al. Status of SuperWASP I (La Palma). *Astron. Nach.* **325**, 565–567 (2004).

61. Jehin, E. et al. TRAPPIST: Transiting Planets and Planetesimals Small Telescope. *The Messenger* **145**, 2–6 (2011).

62. Barkaoui, K. et al. Discovery of three new transiting hot Jupiters: WASP-161 b, WASP-163 b, and WASP-170 b. *Astron. J.* **157**, 43 (2019).

63. Garcia, L. J. et al. PROSE: a Python framework for modular astronomical images processing. *Mon. Not. R. Astron. Soc.* **509**, 4817–4828 (2021).

64. Burdanov, A., Delrez, L., Gillon, M. & Jehin, E. in *Handbook of Exoplanets* (eds Deeg, H. J. & Belmonte, J. A.) 130 (Springer, 2017).

65. Delrez, L. et al. SPECULOOS: a network of robotic telescopes to hunt for terrestrial planets around the nearest ultracool dwarfs. *Proc. SPIE* **10700**, 107001I (2018).

66. Burdanov, A. Y. et al. SPECULOOS Northern Observatory: searching for red worlds in the northern skies. *Publ. Astron. Soc. Pac.* **134**, 105001 (2022).

67. Demory, B. O. et al. A super-Earth and a sub-Neptune orbiting the bright, quiet M3 dwarf TOI-1266. *Astron. Astrophys.* **642**, A49 (2020).

68. Stumpe, M. C. et al. Kepler presearch data conditioning I—architecture and algorithms for error correction in Kepler light curves. *Publ. Astron. Soc. Pac.* **124**, 985 (2012).

69. Smith, J. C. et al. Kepler presearch data conditioning II—a Bayesian approach to systematic error correction. *Publ. Astron. Soc. Pac.* **124**, 1000 (2012).

70. Stumpe, M. C. et al. Multiscale systematic error correction via wavelet-based bandsplitting in Kepler data. *Publ. Astron. Soc. Pac.* **126**, 114 (2014).

71. Baranne, A. et al. ELODIE: a spectrograph for accurate radial velocity measurements. *Astron. Astrophys. Suppl. Ser.* **119**, 373–390 (1996).

72. Zechmeister, M. & Kürster, M. The generalised Lomb–Scargle periodogram. A new formalism for the floating-mean and Keplerian periodograms. *Astron. Astrophys.* **496**, 577–584 (2009).

73. Doyle, A. P., Davies, G. R., Smalley, B., Chaplin, W. J. & Elsworth, Y. Determining stellar macroturbulence using asteroseismic rotational velocities from Kepler. *Mon. Not. R. Astron. Soc.* **444**, 3592–3602 (2014).

74. Bruntt, H. et al. Accurate fundamental parameters for 23 bright solar-type stars. *Mon. Not. R. Astron. Soc.* **405**, 1907–1923 (2010).

75. Gray, R. O. & Corbally, C. J. An expert computer program for classifying stars on the MK spectral classification system. *Astron. J.* **147**, 80 (2014).

76. Eastman, J., Gaudi, B. S. & Agol, E. EXOFAST: a fast exoplanetary fitting suite in IDL. *Publ. Astron. Soc. Pac.* **125**, 83 (2013).

77. Gelman, A. & Rubin, D. B. Inference from iterative simulation using multiple sequences. *Stat. Sci.* **7**, 457–472 (1992).

78. Gelman, A., Carlin, J. B., Stern, H. S. & Rubin, D. B. *Bayesian Data Analysis* 2nd edn (Chapman & Hall, 2003).

79. Henden, A. A. et al. VizieR Online Data Catalog: AAVSO Photometric All Sky Survey (APASS) DR9 (Henden+, 2016). *VizieR Online Data Catalog* https://ui.adsabs.harvard.edu/abs/2016yCat.2336....0H (2016).

80. Cutri, R. M. et al. *2MASS All Sky Catalog of Point Sources* (2003); https://ui.adsabs.harvard.edu/abs/2003tmc..book.....C

81. Wright, E. L. et al. The Wide-field Infrared Survey Explorer (WISE): mission description and initial on-orbit performance. *Astron. J.* **140**, 1868–1881 (2010).

82. Stassun, K. G. & Torres, G. Evidence for a systematic offset of −80 µas in the Gaia DR2 parallaxes. *Astrophys. J.* **862**, 61 (2018).

83. Schlafly, E. F. & Finkbeiner, D. P. Measuring reddening with Sloan Digital Sky Survey stellar spectra and recalibrating SFD. *Astrophys. J.* **737**, 103 (2011).

84. Asplund, M., Grevesse, N., Sauval, A. J. & Scott, P. The chemical composition of the Sun. *Annu. Rev. Astron. Astrophys.* **47**, 481–522 (2009).

85. Schwarz, G. Estimating the dimension of a model. *Ann. Stat.* **6**, 461–464 (1978).

86. Claret, A. & Bloemen, S. Gravity and limb-darkening coefficients for the Kepler, CoRoT, Spitzer, uvby, UBVRIJHK, and Sloan photometric systems. *Astron. Astrophys.* **529**, A75 (2011).

87. wangenmarkers, E.-J. A practical solution to the pervasive problems of *p* values. *Psychon. Bull. Rev.* **14**, 779–804 (2007).

88. Maxted, P. F. L. et al. Five transiting hot Jupiters discovered using WASP-South, Euler, and TRAPPIST: WASP-119 b, WASP-124 b, WASP-126 b, WASP-129 b, and WASP-133 b. *Astron. Astrophys.* **591**, A55 (2016).

89. Jontof-Hutter, D., Dalba, P. A. & Livingston, J. H. TESS observations of Kepler systems with transit timing variations. *Astron. J.* **164**, 42 (2022).

90. Anderson, D. R. et al. Thermal emission at 4.5 and 8 μm of WASP-17b, an extremely large planet in a slightly eccentric orbit. *Mon. Not. R. Astron. Soc.* **416**, 2108–2122 (2011).

91. Lam, K. W. F. et al. From dense hot Jupiter to low-density Neptune: the discovery of WASP-127b, WASP-136b, and WASP-138b. *Astron. Astrophys.* **599**, A3 (2017).

92. Hartman, J. D. et al. HAT-P-65b and HAT-P-66b: two transiting inflated hot jupiters and observational evidence for the reinflation of close-in giant planets. *Astron. J.* **152**, 182 (2016).

93. Demory, B.-O. & Seager, S. Lack of Inflated radii for Kepler giant planet candidates receiving modest stellar irradiation. *Astrophys. J. Suppl. Ser.* **197**, 12 (2011).

Author contributions

K.B. led the project and performed and interpreted the global analyses with support from F.J.P. and M. Gillon. F.J.P. led the interpretation of the results and writing of the paper. P.N. and J.d.W. performed the assessment of atmospheric characterization suitability. C.H., O.T., D.R.A., S.U. and R.G.W. performed the WASP-South observation and data reduction. C.D., R.H. and S.M. performed planet interior models and interpretation of the results. B.S., V.V.G., P.F.L.M., A.S. and M. Ghachoui performed spectroscopic data, stellar evolutionary models and SED analysis. L.D.N., F.B. and M.L. performed radial velocity measurements. E.J., E.D., C.A.M. and P.P.P. performed photometric follow-ups using TRAPPIST-South and SPECULOOS-South facilities and data reduction using Prose. All co-authors read and commented on the paper and helped with its revision.

Competing interests

The authors declare no competing interests.

Additional information

Supplementary information The online version contains supplementary material available at https://doi.org/10.1038/s41550-024-02259-y.

Correspondence and requests for materials should be addressed to Khalid Barkaoui or Francisco J. Pozuelos.

Peer review information *Nature Astronomy* thanks Thomas Wilson and the other, anonymous, reviewer(s) for their contribution to the peer review of this work.

Reprints and permissions information is available at www.nature.com/reprints.

[1]Astrobiology Research Unit, Université de Liège, Liège, Belgium. [2]Oukaimeden Observatory, High Energy Physics and Astrophysics Laboratory, Faculty of sciences Semlalia, Cadi Ayyad University, Marrakech, Morocco. [3]Department of Earth, Atmospheric and Planetary Science, Massachusetts Institute of Technology, Cambridge, MA, USA. [4]Instituto de Astrofísica de Canarias (IAC), La Laguna, Spain. [5]Instituto de Astrofísica de Andalucía (IAA-CSIC), Granada, Spain. [6]Astrophysics Group, Keele University, Staffordshire, UK. [7]Observatoire de Genève, Université de Genève, Sauverny, Switzerland. [8]European Southern Observatory, Garching bei München, Germany. [9]Department of Astrophysics, University of Zürich, Zurich, Switzerland. [10]Space Sciences, Technologies and Astrophysics Research (STAR) Institute, Université de Liège, Liège, Belgium. [11]Center for Space and Habitability, University of Bern, Bern, Switzerland. [12]Instituto de Astrofisica e Ciencias do Espaco, Universidade do porto, CAUP, Porto, Portugal. [13]Department of Physics, University of Warwick, Coventry, UK. [14]LESIA, Observatoire de Paris, CNRS, Université Paris Diderot, Université Pierre et Marie Curie, Paris, France. [15]Université Paris-Saclay, Université Paris Cité, CEA, CNRS, AIM, Paris, France. [16]Center for Computational Astrophysics, Flatiron Institute, New York, NY, USA. [17]Department of Astrophysical and Planetary Sciences, University of Colorado Boulder, Boulder, CO, USA. [18]Cavendish Laboratory, Cambridge, UK. [19]School of Physics and Astronomy, University of Birmingham, Edgbaston, Birmingham, UK. [20]Space Forge, Cardiff, UK. [21]Centre for Exoplanets and Habitability, University of Warwick, Coventry, UK. ✉e-mail: khalid.barkaoui@uliege.be; pozuelos@iaa.es